SAND2013-8798C

Using PIV Measurements to Determine the Role of the In-cylinder Flow Field for Stratified DISI Engine Combustion

Wei Zeng & Magnus Sjöberg
Sandia National Laboratories

David Reuss
Sandia National Laboratories, University of Michigan

Abstract

This study uses high-speed particle image velocimetry (PIV) and spray-Mie imaging to determine the role of the in-cylinder gas flow for combustion in a stratified-charge direct-injection spark-ignited (DISI) engine, operated on E70 fuel. Engine-speed sweeps show that both the combustion rate and cyclic variability for highly stratified operation react very differently compared to traditional well-mixed operation. To clarify why, the in-cylinder flows are assessed as the engine speed is doubled from 1000 to 2000 rpm.

The PIV measurements reveal that the spatially averaged gas-flow speed before TDC at 2000 rpm is twice that of 1000 rpm. This correlates well with the observed doubling of the heat-release rate (in kW) for well-mixed operation. In contrast, for stratified operation the heat-release rate (in kW) increases by only 16% when the engine speed is doubled. This is comparable with the measured 24% increase of flow speeds after injection. Analysis shows that the in-cylinder flow after fuel injection is dominated by the spray-induced momentum. Overall, these results support the hypothesis that for stratified operation, the combustion rate is primarily governed by the fuel/air-mixing rates associated with fuel injection. The primary effect of the in-cylinder flow field generated by the intake and compression strokes is to increase cyclic variability of the combustion rate of this spray-guided combustion system. The spray-Mie imaging reveals that the momentum of the gas flow generated by the intake and compression strokes becomes so strong at 2000 rpm that it even causes a substantial increase of the cyclic variability of the liquid spray.

1. Introduction

In the light of constrained petroleum supply and anthropogenic climate change [1], increased engine efficiency and alternative fuels are of interest. Motivated by potential for high thermal efficiency [2], this study focuses on the combustion in a stratified-charge spray-guided (SG) direct-injection spark-ignited (DISI) engine. For lean and stratified operation, low engine-out NO_x and soot emissions must be achieved to avoid expensive aftertreatment technology in markets with stringent exhaust legislation. Recent studies demonstrated the potential of E85 fuel to enable clean and efficient stratified combustion [3, 4] in an engine with a spray-guided combustion system by igniting the leading edge of the spray (head ignition). That study highlighted the challenging trade-off between a reduction of NO_x emissions and the appearance of partial-burn cycles. Furthermore, spark-plasma imaging in [3] revealed a correlation between flow direction and partial burns, showing that the in-cylinder flow field generated by the intake and compression strokes matters for the stratified combustion process.

The in-cylinder flow field generated by the intake and compression stroke interacts with the flow patterns being induced by the fuel-injection process. A modest literature survey did not reveal any consensus on the role of the in-cylinder flow field for spray-guided SI combustion. Furthermore, no publications were found that explicitly show what factors govern the combustion rate for spray-guided stratified SI combustion. Discussions of the mode of combustion are also rare. The work by Drake et al. [5] is the only paper found that shows data of the relative fraction of the combustion taking place in fully premixed regions, and in mixing-controlled zones, respectively. However, that work does not discuss what controls the combustion rate in these two regions.

In work by Honda *et al.* [6], it is concluded that it is important to have a high penetration-strength of the fuel jet so that the mixture formation is less affected by the air flow in the cylinder. This conclusion implies that the in-cylinder air flow

may not play an essential role for the combustion for that particular spray-guided combustion system and that its effect on the fuel/air mixing should be minimized. Also the work by Schwarz et al. [7] emphasizes that for enabling stratified operation at high engine speeds, it is important to ensure a stable fuel spray despite influence of in-cylinder charge motion.

This dearth of information regarding fundamental aspects of spray-guided stratified-charge combustion stands in strong contrast with the wealth of fundamental combustion knowledge for both traditional premixed SI combustion and Diesel combustion [8]. There are several reasons why a clear understanding of the role of the in-cylinder flow field is important for stratified SI combustion; first, it would provide a cornerstone of a conceptual model of spray-guided SI combustion that can guide both experimentalists and developers of computer models. Second, it has potential to reveal the cause of sporadic partial-burn cycles. To address this, concurrent work in Ref. [9] used systematic all-metal engine performance testing to start unraveling the role of the in-cylinder flow field for a stratified-charge SI engine, both regarding combustion rate and combustion stability.

The experimental results in Ref. [9] allowed formulation of two hypotheses:

1. The combustion rate for highly stratified SI combustion is primarily governed by the fuel/air-mixing rates associated with the fuel-injection process.
2. The role of the in-cylinder flow field generated by the intake and compression strokes is primarily its stochastic influence on the fuel/air mixing, causing cycle-to-cycle variations of the spray-guided stratified combustion.

The latter hypotheses is in line with the wording found in the gasoline work by Honda *et al.* [6], as discussed above, but it was formulated completely independently of that study. The metal engine results in Ref. [9] show that the cyclic variability increases with increasing engine speed. This demonstrates the need to manage the stochastic processes during stratified combustion, which are expected to be strongly affected by the in-cylinder flow development and its cycle-to-cycle fluctuations. There has been a strong effort within the stratified SG DISI combustion research community to identify potential causes of cyclic variation. Spark emission spectroscopy techniques [10] have revealed that overly lean mixtures near the spark plug at the time of ignition are strongly correlated with the occurrence of partial burn and misfire cycles. Electrical discharge phenomena such as spark plasma extinguishment, multiple spark restrikes, surface sparks, and lower spark energy imparted on the mixture have been identified as causes of partial burn and misfire cycles by Fansler *et al*. [11]. They also utilized light-scattering imaging to reveal that local flow velocity fluctuations can cause unfavorable spark motion [12], which leads to misfire. Peterson *et al*. [13] conducted a more comprehensive study of effects of cyclic variability using high-speed imaging of fuel, flow and flames to investigate the causes of rare misfires and partial burns in a stratified SG DISI engine fueled with gasoline, which requires ignition of the trailing edge of the spray. This work [13] affirmed the work of Fansler that the flow field close to the spark plug is one of the important causes of cyclic variation of the stratified SG DISI combustion. In particular, flow fields that directed the flame kernel away from the fuel cloud prevented sufficient flame propagation into the flammable mixture and showed a tendency to generate misfires or partial burns. This previous investigation [13] in a DISI engine was carried out at relatively low engine speeds (less than 1000 rpm). Hence, further investigations are needed to clarify the role of in-cylinder flows at higher engine speeds and how these flows influence both the burn rate and cyclic variability of SG stratified-charge engines. Spray characterizations in a stratified SG DISI engine carried out by Fansler and Drake [12] showed that cyclic fluctuations in spray macroscopic structure are small. Therefore, causality between the spray and the observed combustion variability could not be affirmed for their particular operating conditions. Further investigations need to clarify the spray characteristics and variability in the engine at different operating conditions since the spray atomization and evaporation processes as well as the fuel-air mixing process are highly dependent on the fuel pressure, fuel temperature, ambient density, ambient temperature, fuel properties, and nozzle geometry, as discussed in Ref. [14-16].

To further the understanding of stratified SI combustion, it may be worthwhile to also examine research efforts related to Diesel combustion, which is inherently stratified. In terms of the in-cylinder flow field, studies based on laser diagnostics and modeling have demonstrated that the in-cylinder flow field plays a pivotal role in the mixture preparation, combustion, and pollutant formation processes in direct-injection Diesel engines. For example, recent measurements made by Miles *et al.* [17], closely coupled with numerical simulations, described well how the flow field affects the combustion under various conditions in diesel engines as injection parameters, swirl and engine speed were varied. They further identified the dominant sources of flow turbulence and the mean flow structures conducive to turbulence generation. However, cycle-to-cycle variations were not discussed in detail, perhaps because it is not considered an important challenge for diesel combustion.

The current optical study seeks to determine the role of the in-cylinder flow field on the combustion in a stratified SG DISI engine, regarding both average heat-release rate and cyclic variability. E70 is the fuel chosen by the current authors for

both the all-metal study [9] and this parallel optical study. This fuel blend is justified by ASTM specifications of Ethanol-Flex Fuel (aka E85) [18], and US DOE's definition of alternative fuels [19]. The latter requires an ethanol-based alternative fuel to contain at least 70% alcohol.

Here, the role of the in-cylinder flow is assessed as the engine speed is doubled from 1000 to 2000 rpm. Of course the flow change due to the change in rpm is confounded by the thermodynamic rate of change during the fixed fuel-injection rate. Thus, particle image velocimetry (PIV) is used to measure properties of the flow, independently. This flow field is captured in a tumble plane in the central part of the piston bowl, which captures the tumble flow generated during the intake stroke and by the late fuel injection. Hence, the swirl flow is not measured in this paper. This optical diagnostic study is conducted at operating conditions determined from continuously-fired all-metal engine testing [9]. The PIV results are complemented by pressure-based heat release analysis, high-speed flame imaging and high-speed light-scattering images of the spray. The diagnostic methods as well as the noise and error of results are discussed in detail. The results include comparisons of the average and cycle-to-cycle velocity without injection and with injection (no ignition). This study will not be able to provide a complete and final assessment of the role of the in-cylinder flow field, but should serve well as a starting point and offer an opportunity to strengthen or reject the two hypotheses presented above.

2. Engine and operations

2.1 Single-cylinder engine

The engine used for the experiments is a single-cylinder four-valve research engine that can be set up in two configurations; an all-metal configuration for continuously fired performance testing, or in a nearly identical optical piston and head configuration for imaging studies. All tests here were conducted with a water-cooled metal cylinder and oil-lubricated metal piston rings. The piston has a moderately deep piston bowl to aid the stratification of fuel. Fig. 1 shows a cross section of the combustion chamber at top-dead-center (TDC) and Fig. 2 shows a picture of the piston top. The piston bowl has a slight cut-out on one side to facilitate a better view into the bowl when the pent-roof side-window on the right-hand side in Fig. 1 is used. Some engine data are given in Table 1. The engine was fueled using an 8-hole injector with a nominal included angle of 60°, and the distance from the injector tip to the spark-plug gap was 13 mm. The injector was oriented such that two of the fuel sprays straddled the spark-plug gap. For all data in this study, one of the intake valves was deactivated to increase in-cylinder swirl and tumble levels, see Table 1.

N_2 dilution was used to lower the intake mole fraction of oxygen [O_2] to simulate the dilution effects of EGR. This charge dilution is important for controlling NO_x emissions. The intake [O_2] being used here (19%) is equivalent to that with 20% external exhaust gas recirculation, but of course does not include the exact chemical composition of real EGR. Air and N_2 were metered with sonic nozzles. For each operating point, the in-cylinder pressure, spark current, intake and exhaust pressure, and fuel pressure were acquired with a 0.1°CA resolution. The apparent heat-release rate (AHRR) was computed from the in-cylinder pressure for each individual cycle using a constant ratio of specific heats (γ) following [8]. For optical diagnostics, the engine was equipped with a concave quartz-window in the piston bowl and a flat quartz-window in the end of the pent-roof section closest to the injector, see Fig. 1c and Fig. 1d, respectively.

As discussed above, this study uses E70 fuel. The E70 fuel was prepared in-house by blending the research-grade gasoline with anhydrous high purity grade ethanol in 30%/70% proportions by volume. The gasoline is Chevron-Phillips research-grade gasoline with an antiknock index of 87. It is a typical gasoline and its specifications can be found in [4,9].

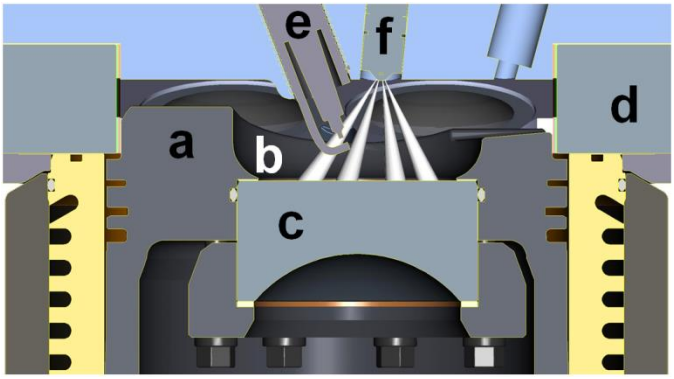

Figure 1 - CAD rendering of cross-section of combustion chamber at TDC with a - piston, b - piston bowl, c - piston-bowl window, d - pent-roof window, e - spark plug, and f - fuel injector.

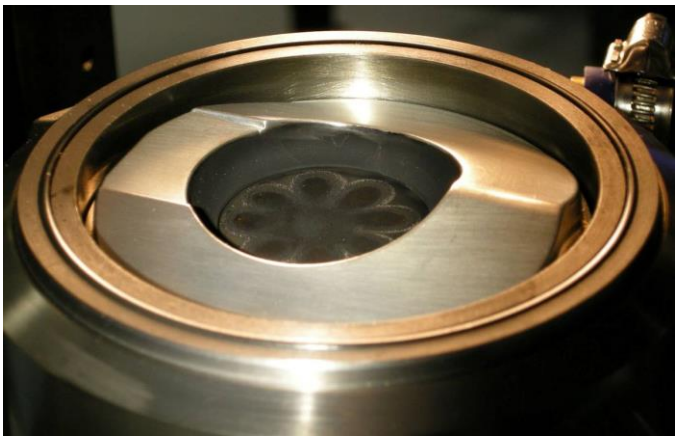

Figure 2 - Picture of piston (in all-metal configuration) and cylinder in its dropped-down position.

Table 1 - Engine specifications

Displacement	0.552 liters
Bore/Stroke	86.0/95.1 mm
Geometric Compression Ratio	12:1
Swirl/Tumble Index (single intake valve)	2.7/0.62
Spark Coil	Bosch, ZS-L 1×1 E
Fuel Injector	Bosch 8-hole w/60° included angle
Hole Size	Stepped-hole, min. dia. = 0.125 mm

2.2 Engine operation with "head" ignition and near-TDC injection

All-metal engine experiments were conducted in Ref. [9] to establish the test conditions for the skip-fired optical-engine experiments performed here; those tests of 500 consecutive cycles demonstrated that near-TDC injection, with head ignition and E70 can achieve ultra-low emissions of NO and relatively high combustion efficiency and stability. Fig. 3 shows two examples of the head ignition strategy. Fig. 4 presents the injection-retard effect on the trade-off between NO emission and combustion efficiency at 1000 rpm as an example to demonstrate the benefits of near-TDC injection. All four test conditions shown in Fig. 4 were operated stably with head ignition at a constant N_2 dilution level rendering $[O_2]_{in}$ = 19%. It clearly shows that retarding the injection timing decreases engine-out NO emission, while the thermal efficiency increases until a certain start of injection (SOI) before the TDC and then decreases. In this case, SOI = -10°CA ATDC (after top dead center) is considered to offer the best trade-off between NO emission and thermal efficiency. This operating point has CA50 = 8°CA.

The comparison of gasoline and E70 in the metal engine [9] revealed that the strategy to use near-TDC injection with head-ignition for E70 produces low NO emissions also as engine speed is increased. As reported [4], the closely-coupled injection and ignition and more injected fuel, required by the lower heating value of ethanol, leads to a combustion event that visually appears to have a finer structure. It is speculated in [4] that the fine structure is possibly indicative of higher turbulence level during ethanol combustion compared to gasoline with tail ignition. This higher turbulence level could contribute to lower NO formation by enhancing the mixing between hot combustion products and cooler unused air.

Figure 5 presents the $IMEP_g$ and the corrected standard deviation (CSD) of $IMEP_g$ as a function of engine speed based on the metal engine experiments [9]. The latter is defined as:

$$\text{CSD of IMEP}_g[\%] = 100 \cdot \frac{\sigma_{IMEP_{g,fired}}}{(IMEP_{g,fired} - IMEP_{g,motored})} \qquad (1)$$

Here, the standard deviation (σ) of $IMEP_g$ for fired operation has been corrected for the heat transfer losses of a motored cycle by being normalized by the difference in average $IMEP_g$ for fired and motored operation. The difference in $IMEP_g$ for fired and motored operation equals the $IMEP_g$ rise caused by the combustion event. This definition allows the combustion stability to be consistently evaluated even for operation with $IMEP_g$ near zero or negative, (*e.g.* idle operation or vehicle coasting).

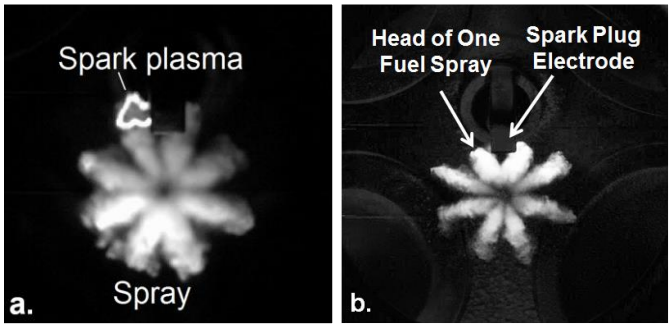

Figure 3 - a) An example of "extreme" head ignition from [3]. b) An example of head ignition used in this work (spark plasma exists behind the spark plug electrode); start of injection (SOI) = -23°CA, spark timing (ST) = -22°CA.

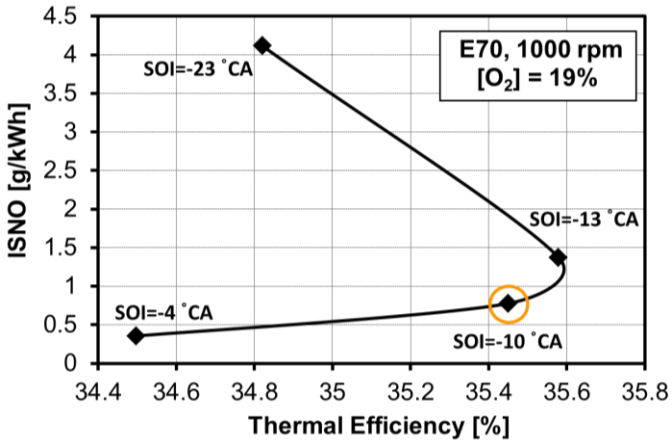

Figure 4 - Trade-off between NO and thermal efficiency using near-TDC injection for E70 [9].

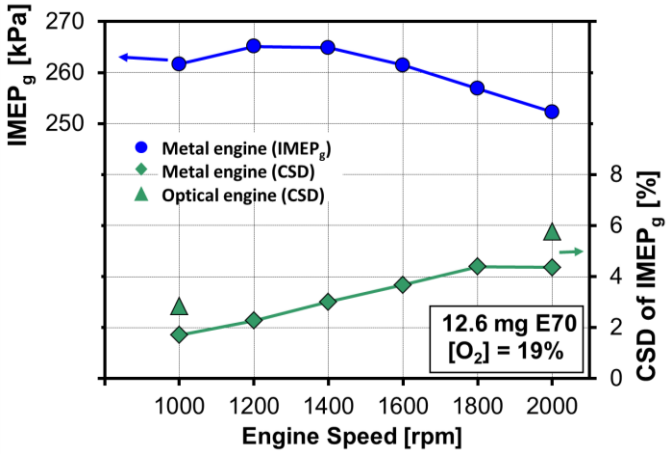

Figure 5 - Effect of engine speed on combustion performance and stability.

For Fig. 5, the fuel mass per cycle, spark energy, intake temperature and pressure, coolant temperature and the N_2 dilution level are kept constant. The spark and injection timings were selected for each speed to achieve head ignition and a 50% burn point (CA50) at 9.0±0.5 °CA ATDC. In this study, SOI is defined to be the crank angle (CA) when the first liquid enters the combustion chamber, as determined by scattered-light imaging via either the piston-bowl window or the pent-roof side window. End of injection (EOI) is the crank angle that the last liquid leaves the injector. Also plotted in Fig. 5 are the data for the two optical-engine-operating conditions shown in Table 2. It can be observed in Fig. 5 that the cyclic variability increases with increasing engine speed. Both the increase of CSD of $IMEP_g$ and the reduction of $IMEP_g$ at the higher speed can be attributed to the appearance of partial burn cycles. It should be noted that the two fired optical data points in Fig. 5 show an increase of CSD of $IMEP_g$ with speed that is quite similar to the all-metal data, providing confidence the optical-engine performance.

Table 2 - Engine operating conditions

Injection pressure	170 bar	
Spark Energy	106 mJ	
Intake Temperature	26-28°C	
Intake Pressure (abs.)	95 kPa	
Coolant Temperature	60°C	
Fuel Type	E70	
EGR/$[O_2]_{in}$	19%	
Injection Duration (command)	0.925 ms	
Fuel Mass	12.6 mg	
Engine Speed	1000 rpm	2000 rpm
Start of Injection	-8°CA	-21°CA
End of Injection	-2°CA	-9°CA
Spark Timing	-7°CA	-19°CA
Average $IMEP_g$	276 kPa	248 kPa
Std. Deviation of $IMEP_g$	9.7 kPa	18.5 kPa
CA50	9.2°CA	9.0°CA

2.3 Operating strategies for optical tests

The optical engine experiments were conducted with both non-fired and fired engine operation at each of the two engine speeds that are listed in Table 2. Measurements included PIV and imaging of spark plasma, broad-band flame luminosity, and Mie-scattering of the liquid spray. The four different data acquisition strategies in Table 3 were used in conjunction with the two cycle sequences described in Figs. 6a and 6b. For non-fired operations, a repeated four-cycle sequence is used. Data "a" correspond to the non-fired non-injected operation with spark discharge and PIV acquisition on every second cycle of the four-cycle sequence. Data "a" demonstrate the evolution of flow field generated by the intake stroke and the flow-spark interaction. However, this paper only presents the PIV results for flow evolution, while the data for understanding the effect of flow field on spark motion are not shown. Data "b" on cycle 3 of the four-cycle sequence have injection but no spark and include PIV and laser-based spray imaging. Data "b" reflect the impact of fuel injection on the flow-field development. Data "c" have PIV, spray illumination, and flame acquisition on the second fired cycle of a Fire2-Skip6 sequence. These data are aimed at investigating flow-field effects on combustion. The dilution, injection, ignition are identical to the pre-established all-metal operating points. The Fire2-Skip6 sequence achieves a 25% duty cycle to reduce the thermal load, with data acquisition during the second fired cycle to ensure proper temperature and composition of the residual gases. Data were acquired for 100 cycles for each of "a", "b", and "c", for a total of 300 cycles per test condition. However, due to space constraints, PIV results for cycles with combustion (data "c") are not presented in this paper. Hence, for data "c", only IMEP, AHRR, and flame imaging are presented.

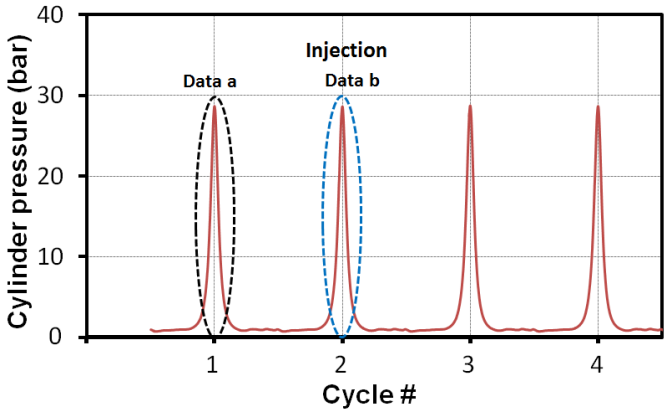

Figure 6a - Data acquisition for non-fired operation; taken at the first (Data "a") and second (Data "b") cycles in each sequence.

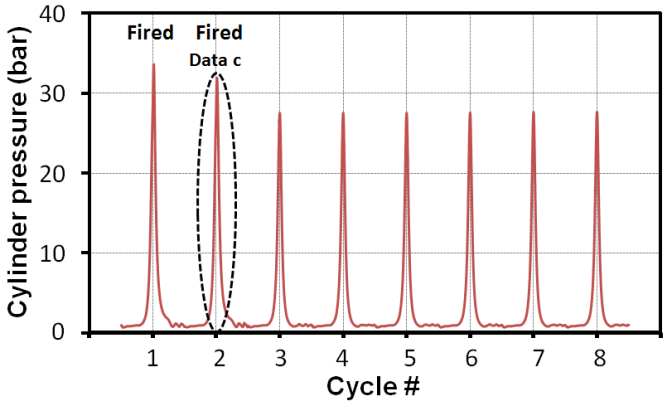

Figure 6b - Fire2-Skip6 sequence for fired operations; data taken at the second cycle (Data "c") in each sequence

In addition, data "d" correspond to two injected but non-ignited operating points with spray illumination only. Data "d" are aimed at understanding the flow effect on the cycle-to-cycle variability of the liquid spray. The operation conditions

for Data "d" are shown in Table 4. The operating condition with the engine speed of 333 rpm provides a weak in-cylinder flow, while the 2000 rpm condition reflects a relatively strong flow-field impact on the liquid spray development. Here, E85 fuel is used for the two special designed operating points. Ideally, E70 fuel should have been used. On the other hand, the latent heat of vaporization is not radically different for E85. It is expected that E85 requires more heat for vaporization, likely leading to a slightly longer liquid spray penetration. The fuel mass per cycle, injection pressure, coolant temperature, intake temperature and pressure are kept constant for the two operating conditions. The electric signal to trigger the injector was fixed at a same crank angle for both engine speeds. Hence, the liquid SOIs differ slightly. It is observed that the peak pressure is dependent on engine speed due to the differences in heat transfer and blow-by at the two speeds, indicating slightly different in-cylinder gas densities and temperatures. Data were acquired for 200 cycles per test condition using an Inject1-Skip3 sequence with spray illumination on the first cycle.

Table 3 - Data acquisition for four injection and spark strategies.

Data	Spark	Injection	PIV	Spray	Flame
a (non-fired)	Yes	No	Yes	No	No
b (non-fired)	No	Yes	Yes	Yes	No
c (fired)	Yes	Yes	No	Yes	Yes
d (non-fired)	No	Yes	No	Yes	No

Table 4 - Non-ignited injection operations for E85 at 333 and 2000 rpm

Injection pressure	170 bar	
Intake Temperature	26-28°C	
Intake Pressure (abs.)	95 kPa	
Coolant Temperature	60°C	
Fuel type	E85	
Injection duration	0.925 ms	
Fuel mass	12.6 mg	
Engine speed	333 rpm	2000 rpm
Start of injection	-22.2°CA	-18.6°CA
Peak pressure	2285 kPa	2715 kPa

3 Optical measurements

High-speed planar PIV, combustion luminosity, and spray images were acquired to understand in-cylinder mixing and combustion processes within the stratified SG DISI engine. Fig. 7 shows the experimental setup of the single-cylinder optical engine with laser-sheet forming optics and two cameras.

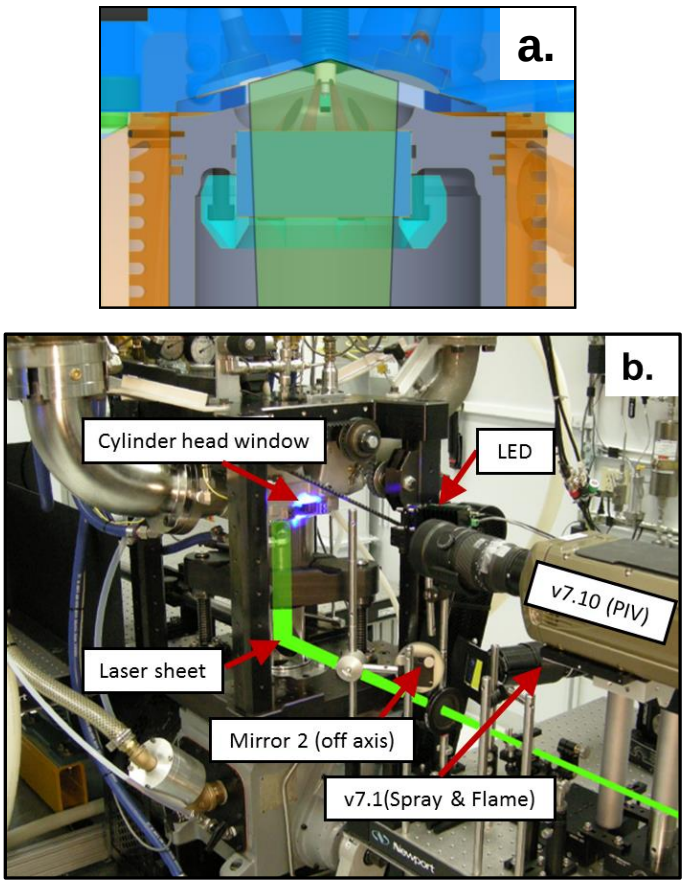

Figure 7 - a) CAD rendering of laser sheet entering via piston-bowl window. b) Experimental setup of the single-cylinder optical engine, laser configuration and two camera optical systems.

3.1 Flame and spray imaging

Simultaneously with PIV, flame and spray images were acquired through the piston-bowl window using a monochrome high-speed Phantom v7.1 camera. This imaging was performed via two mirrors; the Bowditch-piston mirror was installed just below the piston and a second mirror was located off axis to avoid blocking the laser sheet (refer to Fig. 7b). For orientation, Fig. 8a presents an image of the combustion chamber, but acquired separately using only the Bowditch mirror. Because of the second mirror with its offset position, the view of the flame and spray images is flipped and slightly angled compared to that of Fig. 8a. To allow presenting a consistent view to the reader, all presented flame images are flipped and rotated slightly. Both mirrors were UV enhanced broad-band mirrors for recording broadband luminosity of spark and flame. The spray imaging was recorded simultaneously (prior to the flame images) using a blue high-intensity LED with 2μs pulse duration, with the volume illumination entering via the pent-roof side-window. Notch filters were installed in front of the lens to reject the laser-light scattering at 532±10 nm. The piston bowl window had a concave (R = 25mm) lower surface to enable a wide angle view into the combustion chamber. The spray images

for Data "b" & "c" and flame images of Data "c" were taken each crank angle, starting at two crank angles before the electric timing of the start of injection.

As a separate measurement for data "d", Mie images were acquired through the piston-bowl window and via a Bowditch mirror using a color high-speed Phantom v611 camera. For each speed listed in Table 5, the crank-angle division between frames was adjusted to maintain a 20 kHz frame rate. At least 22 spray images were acquired for each of the 200 injections, spanning from SOI to EOI. Spray illumination was provided via the pent-roof side-window using a broad light beam from a green high-intensity LED, using a 4μs pulse-duration.

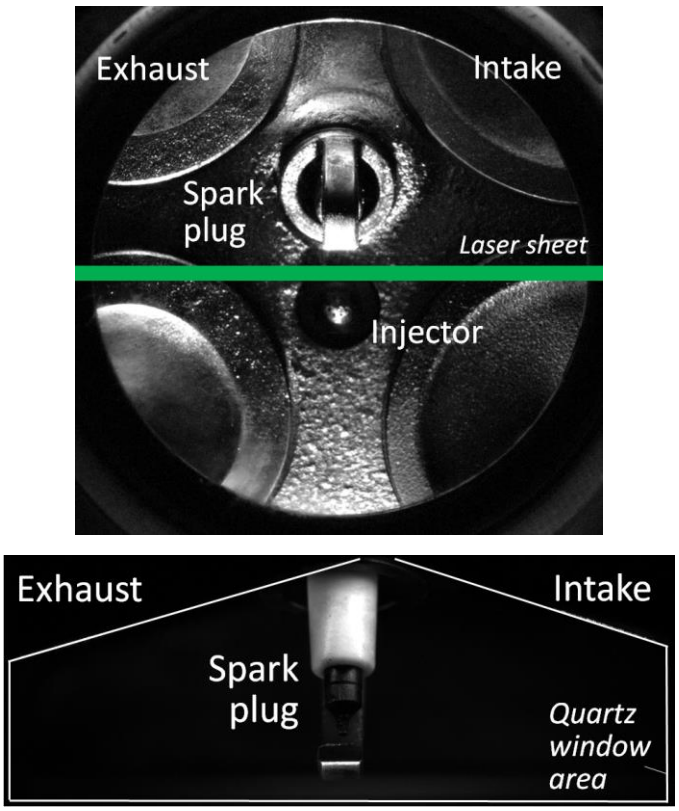

Figure 8 - a) Camera field-of-view for flame imaging (top, via piston window). b) Camera field-of-view for high-speed PIV (bottom, via cylinder head window).

Table 5 - PIV setting and post-processing parameters

Interrogation window size	128×128 to 32×32
Overlap	50%
Spatial resolution of interrogation window	0.98 mm
Magnification	0.75
Field of view	46.9×17.2 mm^2
Frame resolution	1200×440
Seeding density	≈10 - 20 particles per 32×32 pixels
Time delay between two frames (Δt)	10 μs
Crank angle resolution of PIV measurement	2.0°CA

3.2 PIV measurements

High-speed PIV measurements were conducted through the pent-roof side-window to provide an instantaneous two-dimensional (2-D) view of the tumble plane. This work focuses on late-injection stratified combustion. Therefore, the velocity was measured every 2°CA, from -69° to 29°CA ATDC, thereby capturing the flow before fuel injection, the fuel injection itself, and post-injection flow corresponding to the timing of the combustion burn-out. The laser used in these experiments is a high-repetition rate frequency-doubled Q-switched dual-cavity ND: YAG 532 nm laser (Quantronix Dual-Hawk) operated at 3 and 6 kHz, producing two pulses every 2.0°CA at 1000 and 2000 rpm, respectively. A Δt of 10 μs was used for both engine speeds, thus providing an identical dynamic range for the comparisons. The full-width-at-half-maximum duration of each laser pulse, was approximately 120 ns. The laser energy was 7 mJ for 1000 rpm and 4 mJ for 2000 rpm. The laser sheet thickness was 2 mm, thereby degrading the in-plane spatial resolution of the 1 mm interrogation spot size. This relatively thick laser sheet is the result of both the poor transform properties the multi-mode laser cavity and the negative-lens piston-bowl window. The laser sheet was introduced into the engine via a 45° Bowditch mirror to form a vertical plane perpendicular to the ridge of the pent roof. The laser-sheet terminated into the firedeck between the spark-plug electrode and the fuel-injector tip. The PIV seed was provided by silicone oil droplets with a nominal diameter of 1 μm, produced with a six-jet atomizer (TSI 9306), with a seeding density of 10 to 20 particles per interrogation volume.

PIV images were recorded by a high-speed CMOS camera (Vision Research Phantom v710). Viewing through the quartz pent-roof window, the camera was angled approximately 9 degrees downwards to see deeper into the piston bowl. The image perspective was not corrected, and the magnification scaled using the known size of the spark plug. Thus, computed vertical velocity components are underestimated by 8%, but this does not affect the conclusions of this study.

Frame straddling was used to record PIV image pairs every 2°CA degrees. Thus, the camera was operated at 6 kHz and 12 kHz framing rates for 1000 and 2000 rpm, respectively, using a 1200×440 pixel image size. A 180 mm lens (with a 27.5 mm extension ring) imaged the 46.9×17.2 mm^2 area shown in Fig. 8b, yielding a 0.75 magnification. Thus, the 32×32 pixels PIV interrogation window provides an in-plane spatial resolution of 0.98 mm, which is sufficient to resolve the expected flow scales in the 1 to 10 mm range [20]. A relatively large f-stop number (f/16) was selected to provide a sufficient depth of focus for the thick sheet.

The PIV images were recorded using the Vision Research PCC software, then imported and processed using LaVision DaVis software to cross-correlate each PIV frame-pair and produce raw vector fields. Three different masks were applied to the camera images prior to the PIV processing. One mask excluded the intrusion of the piston. A second masked excludes areas of high surface scatter. A third dynamic mask excluded areas where the fuel spray was present. During fuel injection the camera is imaging through the fore-ground fuel jets. These lead to multiple optical effects, including strong scattering of the laser light, and local saturation of the image sensor and therefore, the vectors located in the spray were removed.

Multi-pass PIV cross-correlation was used, with two passes for each reduction in window size from 128×128 to 32×32 pixels. 50% overlap was used resulting in vectors on a 0.5 mm grid spacing in both directions. Next, a five-step post-processing procedure was performed to remove obviously bad vectors and to clean up the final vector field: 1) Vectors with a first-to-second correlation-peak ratio less than 1.4 are deleted. 2) A bad-vector removal process is implemented where the median and Root-Mean-Square (RMS) of the velocities of the vector and its eight immediate neighbors are computed. Any vector with a median velocity that is greater than two times the RMS is removed. 3) If there are at least three neighboring vectors, the median velocity and RMS are calculated again and each vector removed earlier is reinserted if the difference between its magnitude and the median velocity is less than three times the RMS of the neighboring vectors. 4) Interpolation is used to fill in removed vectors by averaging all active neighboring vectors, if at least two neighboring vectors are active. 5) The velocity fields are smoothed using a 3×3 vector filter for the active-vector area.

As a result of the PIV interpolation and post-processing, the total active-vector number in each vector field depends on the crank angle. Figures 9a and 9b show the total number of active vectors at 1000 and 2000 rpm, in each of three randomly selected cycles, with and without fuel injection. For the no-injection cases, the number of active vectors shows a symmetric dip around TDC due to the piston reducing the field of view. For the injected cases, the number of active vectors was further reduced due to the spray area mask and the number of active vectors shows a sudden decrease after the start of injection. The number of active vectors for operation with injection at 1000 rpm does not differ much between the three cycles shown in Fig. 9a, indicating a repeatable spray structure. However, for the 2000 rpm case in Fig. 9b, the variation during injection is enlarged, probably because of a relatively high cyclic variability of the spray structure. These effects of flow on the liquid part of the fuel jet will be addressed separately in section 4.5.

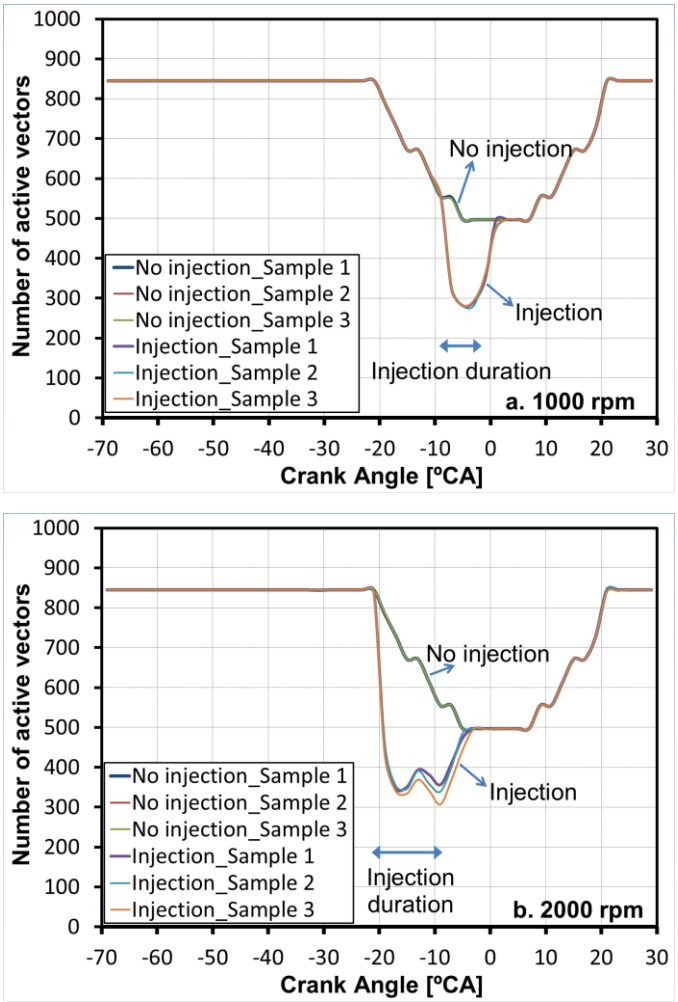

Figure 9 - Number of active vectors in each vector field of three randomly selected cycles at (a) 1000 rpm and (b) 2000 rpm.

3.3 Velocity-error analysis

PIV measurement accuracy and resolution depends on size and pixel resolution of interrogation window, particle image size, particle number density, thickness of laser sheet, and time between two image-frames (Δt) [21]. In this study, the PIV experimental settings in Table 5 are designed to achieve the optimal velocity dynamic range by using particle images of 3-4 pixel diameter, in a 32x32 pixel interrogation size, and Δt to achieve a maximum displacement of 8 pixels. The maximum in-plane particle displacements should not exceed eight pixels to avoid biasing the velocity towards low values. Here, 8 pixels correspond to a velocity magnitude of 31 m/s. The most optimistic velocity resolution is 0.15 pixel RMS based on the RMS noise of real images [22]. Thus, the measured velocities here have an RMS uncertainty of 0.58 m/s. Following the analysis of Abraham *et al.* [23] for cycle-resolved high-speed PIV, Figs. 10a and 10b present the maximum and minimum measured velocity as a function of crank angle for three randomly chosen cycles with injected

operation at 1000 rpm and 2000 rpm (data "b" in Table 3). The maximum velocity of the liquid spray is higher than 150 m/s, but the spray has been masked and is not included. Thus, Figs. 10a and 10b show only the gas velocity, which marginally exceeds the 8 pixel limit near -10°CA. Of course measured velocities below 0.58 m/s are a convolution of the velocity and the measurement noise.

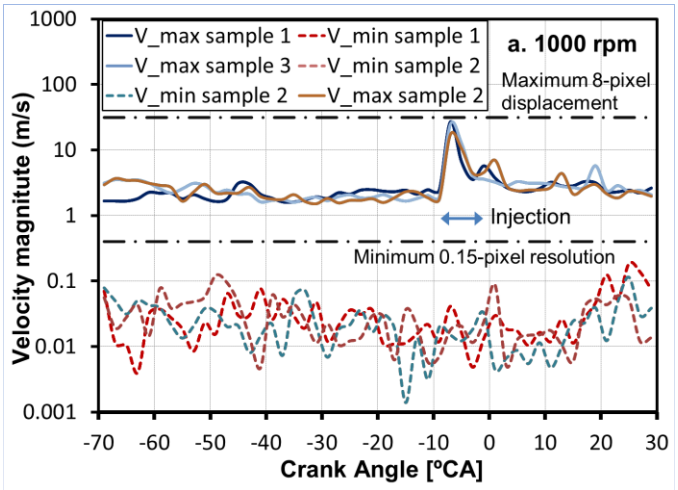

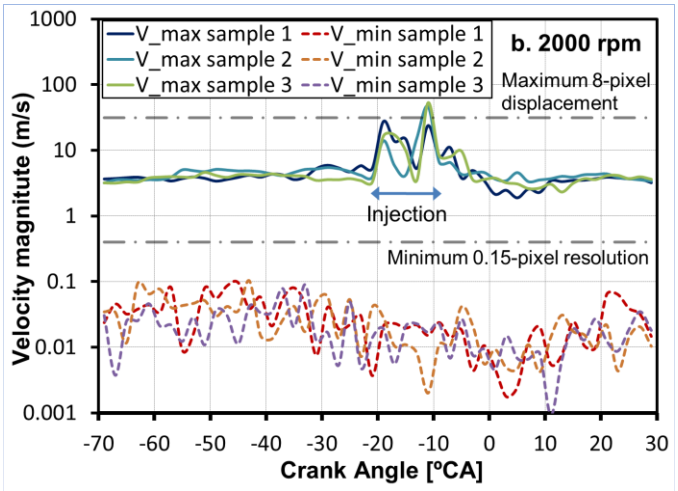

Figure 10 - Maximum and minimum velocity values in each vector fields observed during three randomly chosen cycles at (a) 1000 rpm and (b) 2000 rpm.

Figures 11a and 11b plot the percentage of vectors dominated by noise as a function of crank angle for the three cycles plotted in each of Figs. 10a and 10b. Here vectors whose magnitude was less than the low-velocity limit or larger than the high-velocity limit were defined as potential noise vectors. The noise vector percentage is defined as the number of noise vectors divided by the total number of active vectors in each vector field. For the data before TDC, the noise vector percentage is relatively low (less than about 25%) for both engine speeds. Analysis shows that all noise vectors have velocities below the 0.15 pixel displacement limit. Thus, Fig. 11 indicates the relative size of the flow field where the flow velocities are so low that they become comparable with the measurement noise. Consistent with this, the noise vector percentage before injection is slightly larger for the lower engine speed. This is due to lower mean flow velocity for the 1000 rpm case. On the other hand, it should be emphasized that both the average flow velocity and average flow energy primarily depend on the vectors above the low-velocity limit, and these vectors account for a majority of the total number of active vectors. Overall, these results indicate that $\Delta t = 10$ µs is an acceptable compromise for both engine speeds.

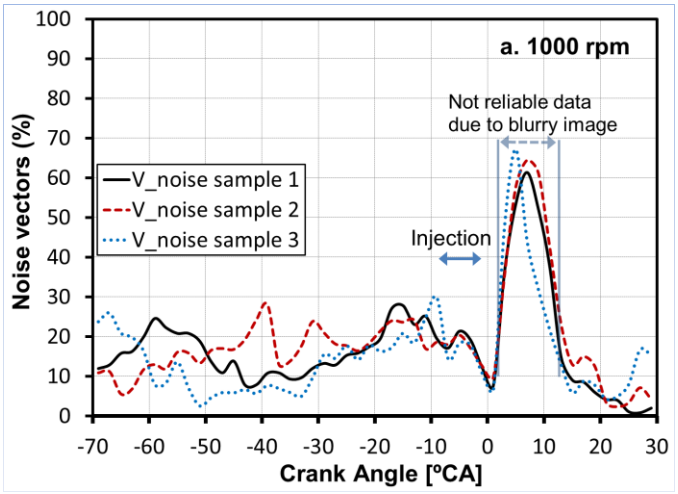

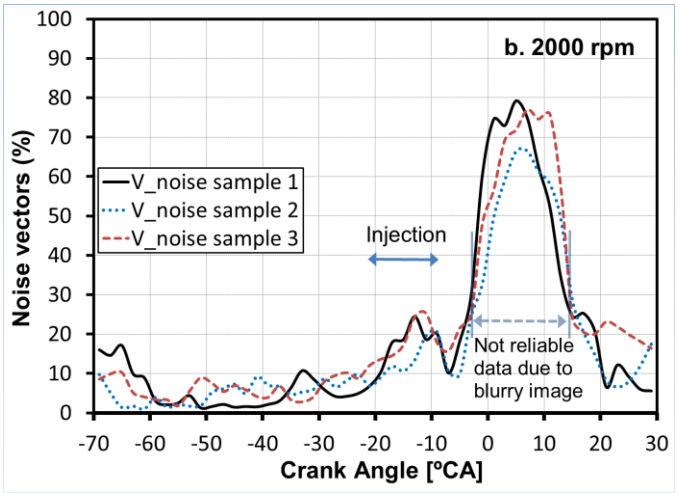

Figure 11 - Noise-vector percentage of the three different cycles as a function of crank angle at (a) 1000 rpm and (b) 2000 rpm

Around TDC, the noise vector percentage becomes extremely high (about 70%). The reason is that the particle images in this range are blurry. These blurry images are likely caused by thermal stratification and density changes as a result of fuel-spray evaporation. The blurry images cause the PIV algorithm to assign wrong values to vectors because of poor cross-correlations. This introduces real errors, not only noise. In this paper, crank-angle ranges with substantial amount of real errors (as indicated in Fig. 11) are excluded from the analysis. After about 13°CA ATDC, the noise vector percentage becomes low again since the mixture temperature and density

decrease during the expansion stroke, and because the thermal and compositional stratifications decrease due to ongoing mixing between fuel and air.

For operation at 1000 rpm, Fig. 11a shows that the crank angle range with unreliable data is shorter than for operation at 2000 rpm. This can be explained by factoring in the longer real time per crank angle at the lower speed because of the same mass injection rate. 1 ms equals 6°CA at 1000 rpm and 12°CA at 2000 rpm. Hence, it takes fewer crank angles at 1000 rpm for the liquid spray to mix with surrounding air and evaporate, and for the charge to become uniform in terms of both composition and temperature.

3.4 Definitions of presented velocity statistics

In this study, PIV measurements provide two velocity components, u and v, in the x- and y- coordinate-directions on a two-dimensional grid with indices i and j, see Eqn. 2.

$$\vec{V}_{i,j,k} = (u_{i,j,k}, v_{i,j,k}) \quad (2)$$

Based on both x- and y- axis components for all individual vectors at a given crank angle, the absolute magnitude and the direction of each vector in the flow field can be generated; one 2-D velocity distribution is measured each cycle, k, of c total cycles. In this study, the magnitude of the velocity is computed, according to Eqn. 3.

$$\left|\vec{V}_{i,j,k}\right| = \sqrt{{u_{i,j,k}}^2 + {v_{i,j,k}}^2} \quad (3)$$

The spatially averaged speed distribution from each cycle is computed as per Eqn. 4.

$$\bar{V}_k = \frac{1}{n\times m}\sum_i^n \sum_j^m \left|\vec{V}_{i,j,k}\right| \quad (4)$$

The spatial-average speed distribution is a scalar measure of the momentum per unit density within the measurement field of view at each crank angle during each cycle.

The ensemble average of the per-cycle spatially-averaged speed is then averaged according to Eqn. 5, which will be referred to as "average flow speed" in this paper.

$$\langle \bar{V} \rangle^c = \frac{1}{c}\sum_k^c \left(\frac{1}{n\times m}\sum_i^n \sum_j^m \left|\vec{V}_{i,j,k}\right|\right) \quad (5)$$

Of course, the ensemble average velocity distributions are computed as usual using Eqn. 6.

$$\langle \vec{V}_{i,j} \rangle^c = \frac{1}{c}\left(\sum_k^c \vec{V}_{i,j,k}\right) \quad (6)$$

4 Results and discussion

4.1 Engine speed effect on combustion performance and stability

Figure 12a presents the cycle averaged (from 100 cycles) crank-angle based heat release rate, AHRR(CA), as a function of CA for operation at 1000 rpm and 2000 rpm. The peak AHRR decreases and the duration (in °CA) increases with engine speed. However, as demonstrated with the metal engine continuously-fired tests of in Ref. [9], the time based AHRR (t) in kW plotted in Fig. 12b shows a somewhat decreased average burn duration and increased peak AHRR with increased engine speed. This shows that the burn rate does not scale with the engine speed as it does for stoichiometric homogeneous flame propagation in well-mixed SI engine combustion [8,9]. Figure 13 presents the variability of AHRR for 100 individual cycles at 1000 rpm and 2000 rpm. Clearly there is a far greater range of combustion variability at the higher engine speed. These ensemble-averaged and individual cycle results in the optical engine are consistent with the continuously-fired metal engine results [9]. These results lead to the hypothesis that spray-guided stratified combustion is mixing controlled, dominated by the momentum of the spray, but that the in-cylinder flow still affects the overall burn rate, in particular cyclic variability. This hypothesis motivated the optical investigation that follows.

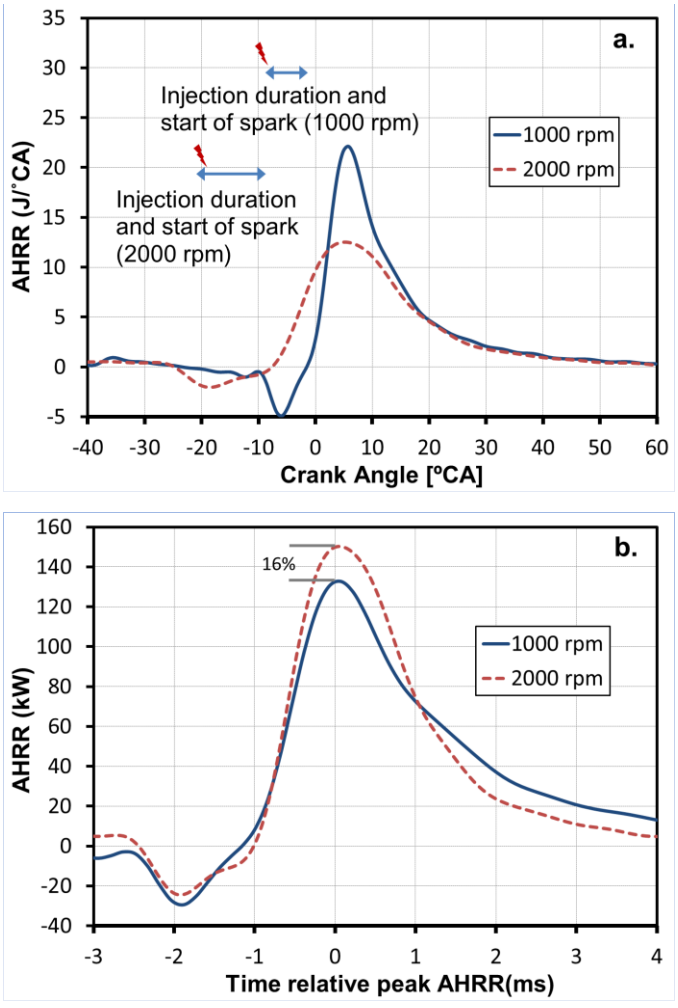

Figure 12 - (a) Crank angle based and (b) time based heat releases at both engine speeds. Time = 0 ms was defined to coincide with peak AHRR.

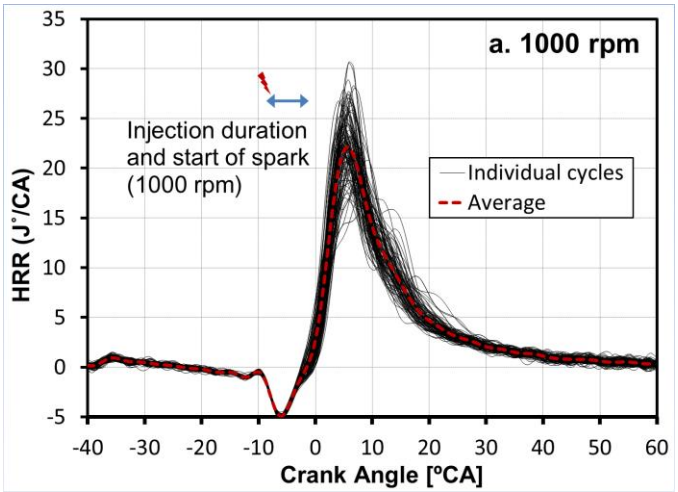

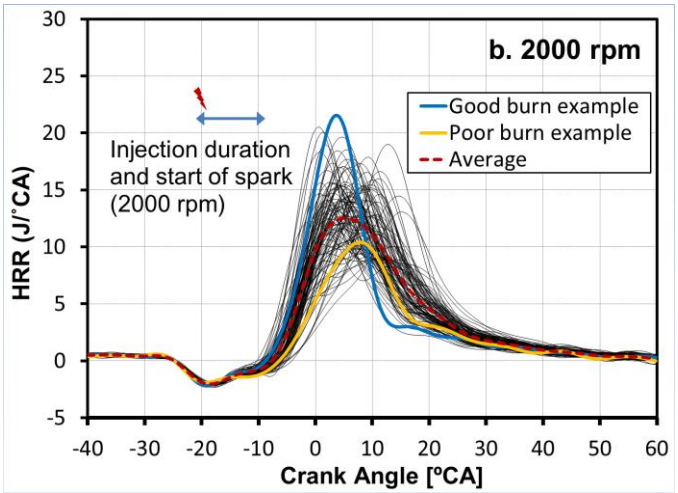

Figure 13 - Cyclic variation of AHRR as a function of CA for 100 cycles at (a) 1000 rpm and (b) 2000 rpm.

As a first step toward understanding burn rate and variability at 2000 rpm, spray and flame images of a poorly burning cycle (IMEPg = 187 kPa) and a well burning cycle (IMEPg = 264 kPa) are shown in Fig. 14 (Data "c"); these correspond to the gold and blue cycles in Fig. 13b. Figure 14 shows crank angles corresponding to ignition and early flame kernel growth, which is known to be very important for combustion stability in stratified SG SIDI engines [24, 25]. The spark and injection timings for both cycles are -19°CA and -21°CA, respectively as per Table 2. Examination of images not shown here confirms that the leading edge of the spray arrives at the spark gap at about -19°CA ATDC, which coincides with the beginning of the spark discharge. Thus, the head-ignition strategy, with its interaction of liquid jets and spark plasma, is observed. After the interaction of spark and spray, a clear early flame kernel is observed at -11 °CA for the good-burn cycle, while it is not observed for the poor-burn cycle until -7°CA, showing a delay of 4°CA. At each crank angle after the early kernel formation, the flame area of the poor burn cycle is always smaller than that of the good burn until the majority of the flame of poor burn cycle reaches the edges of the piston bowl. Thus, the combustion images in Fig. 14 demonstrate that the combustion variability is already present during the ignition and early flame kernel development. The in-cylinder flow is expected to be one of the important factors responsible for the differences observed in ignition and early flame kernel propagation between the poor and good burns.

4.2 Ensemble averaged flow structure

The gas flow prior to injection in this pent-roof engine is a combination of moderately strong swirl and tumble ratios of 2.7 and 0.6, respectively, based on steady-state flow tests. The swirl and tumble flow near TDC is expected to be altered by the momentum of the fuel-injection. However, the interactions between the gas flow and spray are expected to be important factors that influence the fuel mixing from cycle to cycle, thereby affecting the combustion stability. This section presents the mean flow with and without injection (no combustion) during the latter part of the compression stroke and the first part of the expansion stroke. Figure 15 shows the measured ensemble-averaged velocity ($\langle \vec{V}_{i,j} \rangle^c$, shown in

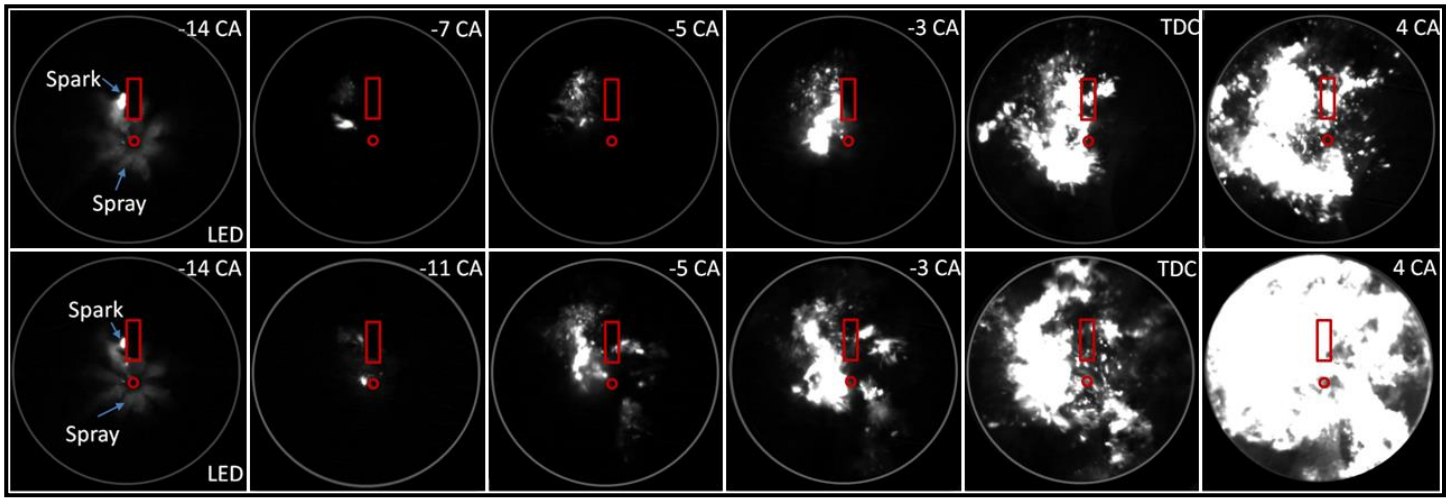

Figure 14 - Flame images of relatively poor burn (Top) and good burn (bottom) cycles.

Eqn. 6) for both engine speeds without fuel injection, demonstrating a clear evolution of the large-scale tumble flow during the latter part of the compression stroke and the early part of expansion stroke. The vortex center of the anticlockwise tumble is first found on the left side of the spark plug and then shifts to the right side, as indicated at -21 and -7°CA ATDC. The tumble is still seen shortly after TDC (11°CA) and it finally disappears due to the piston induced expansion. A similar tumble flow structure is observed for both engine speeds, and it is found that the ensemble-averaged flow velocities scale nearly linearly with engine speed.

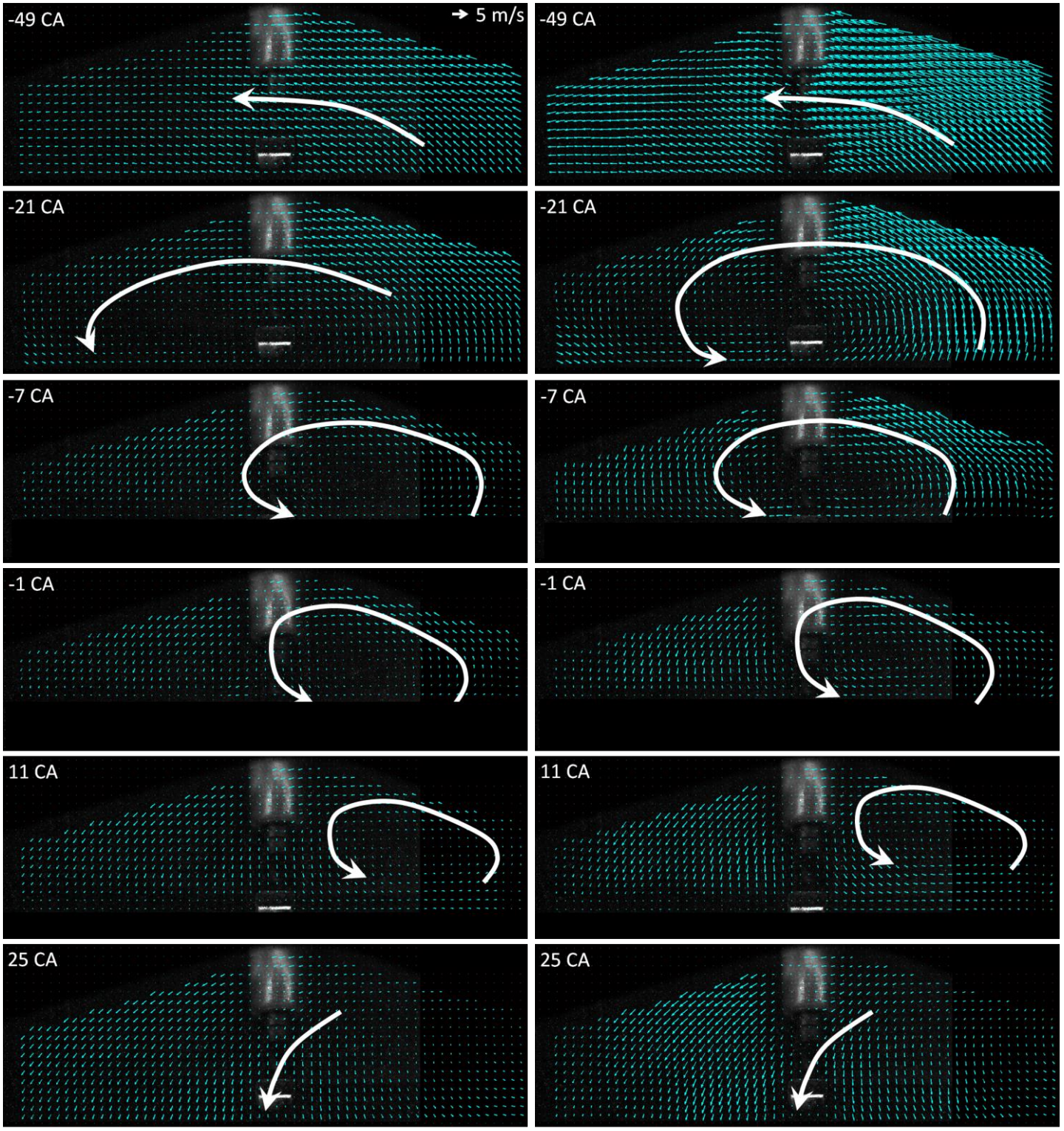

1000 rpm **2000 rpm**

Figure 15 - Mean flow structures of non-fired operations without injection from Data "a" (piston blocks portion of view at -7 to 11°CA).

Figure 16 presents the impact of the fuel spray on the mean flow structure (based on Data "b"). The laser sheet illuminated both the liquid spray and the PIV-seeds during the injection process, hence the flow and spray structures are imaged simultaneously. The number of active vectors varies between cycles because of both the masking and vector removal described in Sect. 3.2. The flow-field images are provided at the same time after SOI for both engine speeds until 1.162 ms ASOI (shortly after the end of injection), as indicated in Fig. 16.

The effect of fuel injection on the mean flow structure is similar for both engine speeds. When the injection occurs, the fuel jets entrain surrounding air that has relatively low momentum. In doing so, this air is moved from the bowl periphery to the center, altering the flow directions. Since the tumble motion generated by the intake system is anticlockwise, the flow on the right side of the spray easily follows the spray trace and indicates a prompt acceleration, while the flow on the left side needs several crank angles before the entrainment flow into the fuel jets is fully established. The flows in both the left- and right-side regions have similar velocity magnitudes after the end of injection. More importantly, it can be seen that after the end of injection, the average vector magnitude of 1000 rpm is close to that of 2000 rpm, as shown in Fig. 16 at 1.162 ms ASOI for both engine speeds. Meanwhile, it is also observed that the flow at 1.162 ms ASOI is significantly different from the flow that is not affected by the injection process for both engine speeds, when comparing the flow field between Figs. 15 and 16 at -1 °CA for 1000 rpm and -7 °CA for 2000 rpm**.** The reason is that the spray momentum, which is expected to be constant for both speeds due to constant mass injection rate and injection pressure, is significantly larger than that of the surrounding air. This shows that the spray-generated flow due to near TDC injection substantially changes the ensemble-averaged tumble flow that was generated by the intake and compression strokes.

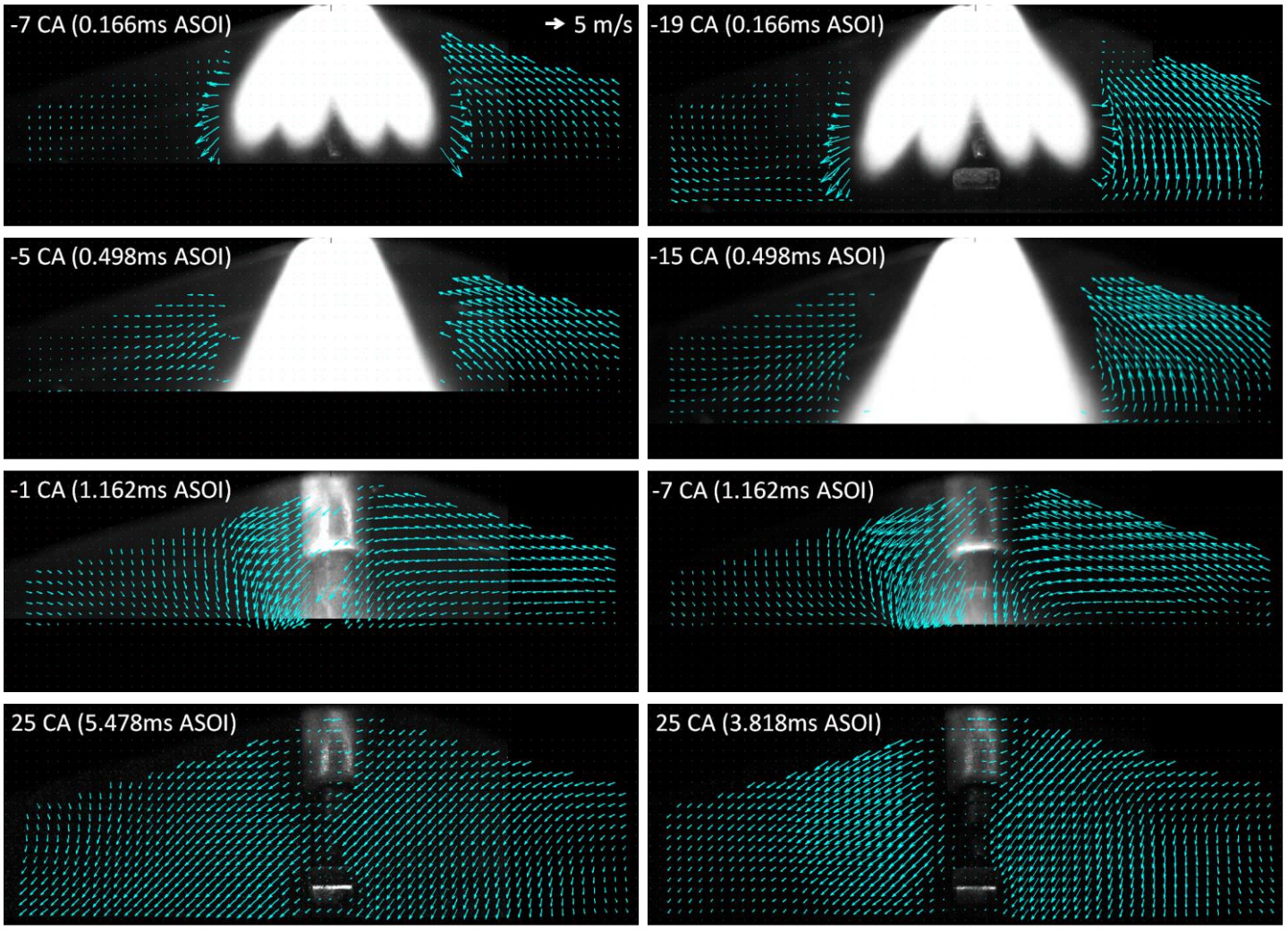

1000 rpm **2000 rpm**

Figure 16 - Mean flow structures of non-fired operations with injection based on Data "b" (piston blocks portion of view at -7, -5, and -1°CA ATDC).

4.3 Scaling of combustion rate with flow speed

As indicated by the average AHRR (t) data shown in Fig. 12b, when the engine speed is doubled, the peak AHRR (t), increases by only 16%. This led to the hypothesis that the burn rate is controlled primarily by fuel-air mixing, and that this mixing is dominated by the spray momentum, albeit influenced by the in-cylinder air flow. To assess this, the spatially averaged speed for each of the 100 cycles is ensemble averaged (Eqn. 5). Figure 17 presents the value of $\langle \bar{V} \rangle^c$ as a function of crank angle for non-fired operation at 1000 rpm and 2000 rpm, both with and without fuel injection. This provides a measure of the average gas momentum in the measurement plane at each crank angle, at both rpm, with and without injection.

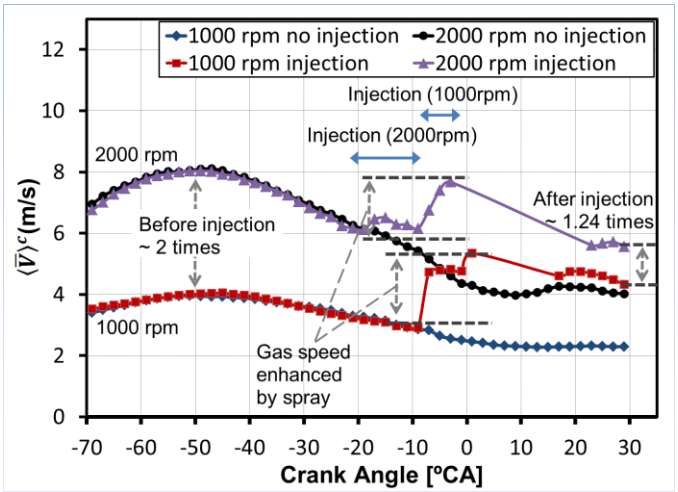

Figure 17 - Evolution of average flow speed for non-fired operation at 1000 rpm and 2000 rpm, both with and without fuel injection (based on Data "a" and "b").

Referring to Fig. 17, $\langle \bar{V} \rangle^c$ peaks at about -50°CA ATDC and dissipates toward TDC. This observation is consistent with Ref. [26], where the transfer of energy from the mean flow to turbulence was shown to occur after -60°CA ATDC. The peak value of $\langle \bar{V} \rangle^c$ at -50°CA for 2000 rpm is about double than that of 1000 rpm and remains two times larger until just prior to injection. This demonstrates that the in-cylinder gas momentum increases approximately linearly with the engine speed. When fuel injection occurs the averaged flow speed ($\langle \bar{V} \rangle^c$) increases by approximately 2 m/s for both 1000 rpm and 2000 rpm. This is consistent with the expectation that the spray momentum during injection is the same and transferred to gas motion with nearly equal efficiency at both engine speeds. During injection, -20 to 0 °CA ATDC, the peak value of $\langle \bar{V} \rangle^c$ in the gas (the liquid is masked) occurring near TDC is about 2 and 1.5 times than that of the gas flow without injection, for 1000 and 2000 rpm, respectively. The net result is that the average speed during injection is only 30% higher for 2000 rpm indicating that the intake-generated gas momentum has a significant contribution, but that the momentum imparted by the spray is dominant over gas-phase momentum forced by the engine speed. Finally, at 29°CA ATDC (which is during the expansion stroke and well after the CA50 point of 9°CA of the comparable combustion tests) the $\langle \bar{V} \rangle^c$ elevated by the spray still persists and is still 24% higher at 2000 compared to 1000 rpm.

Figure 17 demonstrates three important points. 1) The magnitude of the intake-generated flow speed is on the order of that imparted by the spray for the two engine speeds. 2) The average flow-speed increase imparted to the gas phase by the spray is independent of the engine speed. 3) After the intake- and spray-induced flows have combined, the ratio of the average flow speed for the two speeds (1.24) is comparable to the AHRR (t)-increase ratio (1.16) shown in Fig. 12b.

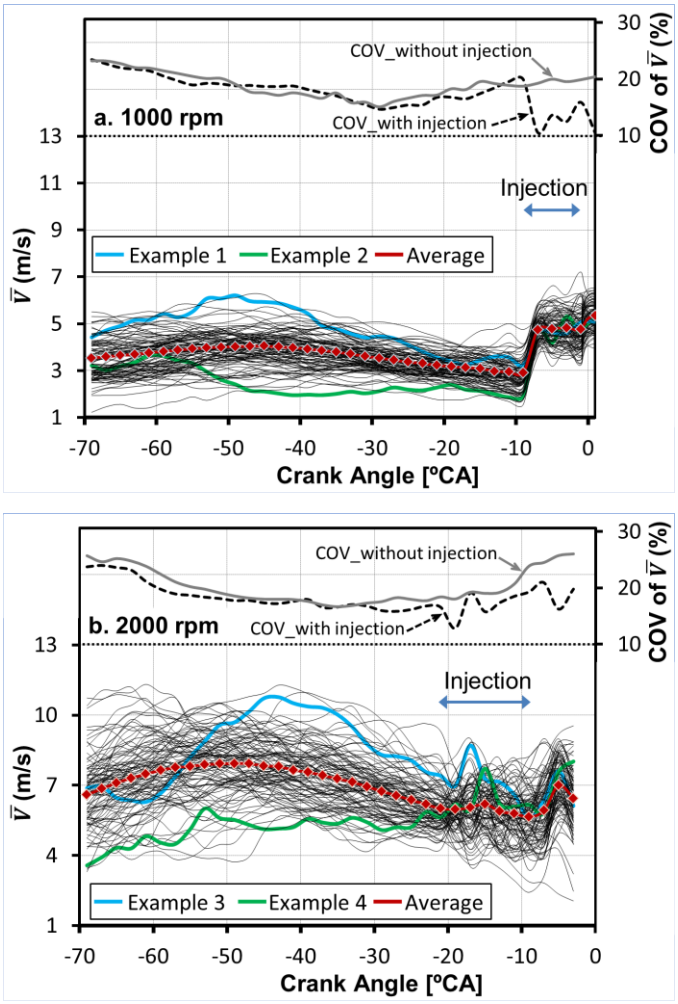

Figure 18 - Cycle-to-cycle variations of spatially averaged flow speed ($\bar{V}_k$) with fuel injection at (a) 1000 rpm and (b) 2000 rpm (based on Data "b").

4.4 Cycle-to-cycle variation of flow field

Figure 18 presents the spatially averaged flow speed ($\bar{V}_k$, as shown in Eqn. 4) of 100 individual cycles with fuel injection

(Data "b") for both engine speeds. Fig. 18 also compares the level of cyclic variability with and without fuel injection as indicated by COV of $\bar{V}_k$. By observing the magnitude of the spread of the individual curves, it can be seen that the cyclic variability increases significantly with engine speed. This is consistent with the variations of engine combustion performance from cycle to cycle observed in Fig. 13. Figure 18 also demonstrates that the relative flow-speed variability (COV of $\bar{V}_k$**)** is reduced by the injection, especially for the lower engine speed. This suggests that the fuel-injection process significantly dominates and decreases variability of the in-cylinder flow. This is also demonstrated by the four instantaneous vector fields in Fig. 19, which shows two examples for each speed: one with high average speed (Examples 1 and 3) and one with low average speed (Examples 2 and 4). These correspond to the blue and green cycles in Fig. 18. At -39°CA ATDC (before injection), the spatially averaged speed and flow structure are significantly different between the two selected examples for each engine speed. This demonstrates large cyclic variations of the intake-induced flow field. After the end of injection, both the flow structures and spatially averaged speeds of the selected examples have become more similar as a result of a strong effect of the fuel injection. Both Fig. 18 and 19 demonstrate the strong interaction between the momentum of the intake-induced flow and spray. However, the large velocity at 2000 rpm (Fig. 18b, Example 3) demonstrates that the tumble structure can be strong enough to persist through the injection event. This then leads to the liquid visualization that follows in Sect. 4.5 to determine if the liquid part of the fuel spray is affected by the measured average flow speed difference.

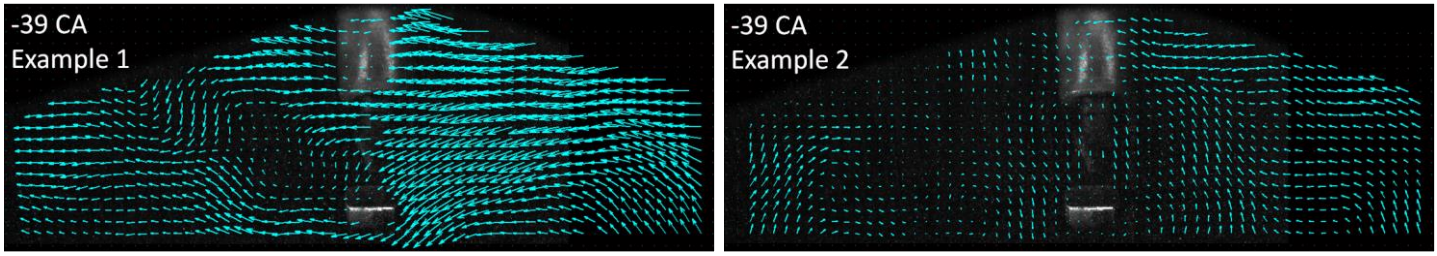

(a) 1000 rpm, before SOI, -39 °CA ATDC

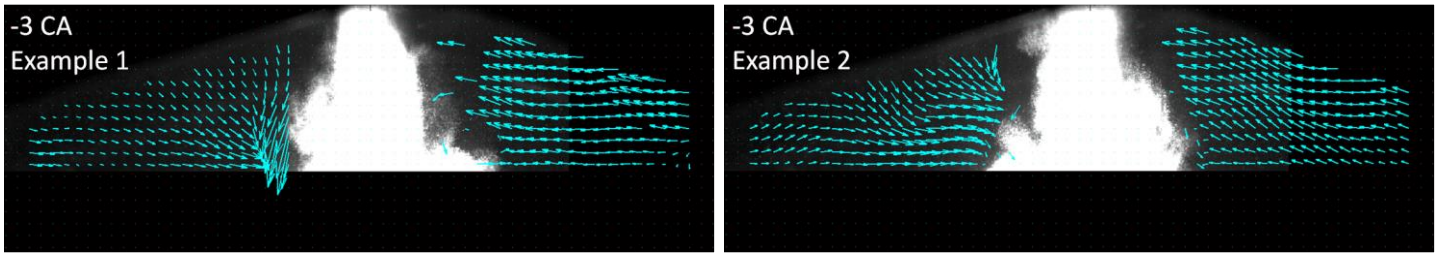

(b) 1000 rpm, after SOI, -3 °CA ATDC

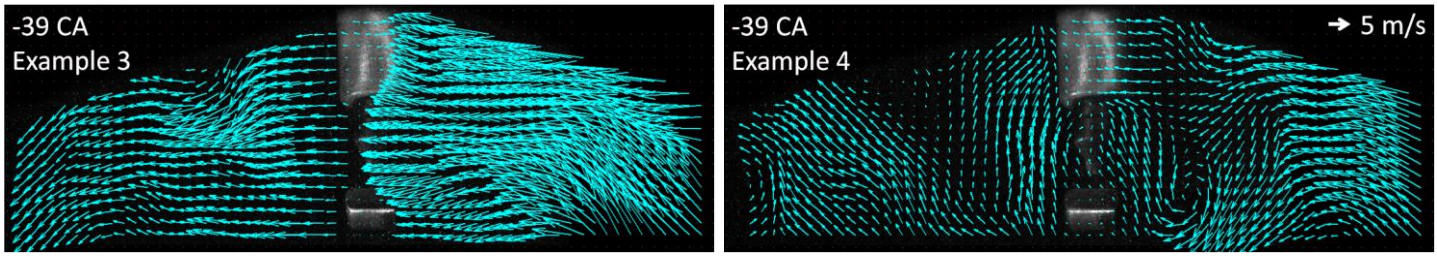

(c) 2000 rpm, before SOI, -39 °CA ATDC

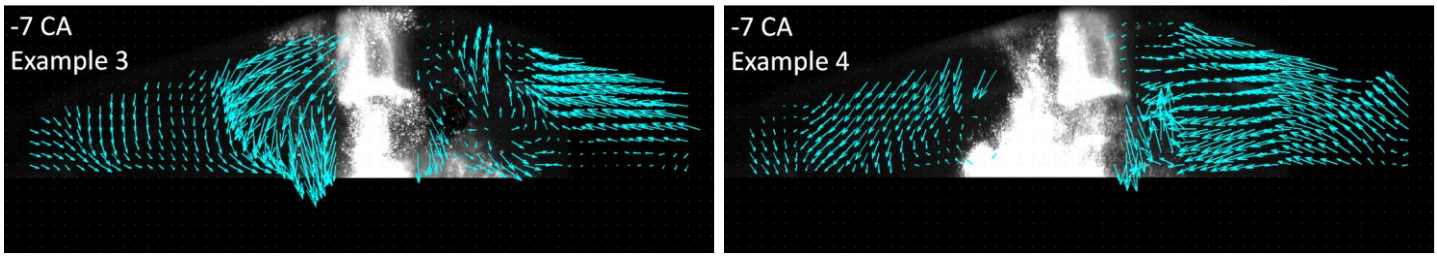

(d) 2000 rpm, after SOI, -7 °CA ATDC

Figure 19 - Flow fields before and after injection for two individual cycles for each engine speed, corresponding to the examples in Fig. 18; Examples 1 and 3 represent a large spatially averaged flow speed, while Examples 2 and 4 correspond to a small spatially averaged flow speed.

4.5 Flow field effect on cyclic variability of the liquid spray

Spray visualization images are shown in Fig. 20 to reveal the effect of in-cylinder gas-flow variability on the spray. These tests (Data "d") were performed using E85, a 0.925 ms injection duration, liquid SOI (the first liquid enters the combustion chamber) = -22.2°CA ATDC at 333 rpm, and liquid SOI = -18.6°CA ATDC at 2000 rpm. The extreme engine speeds (and thus large differences of the in-cylinder flow velocities) were chosen to show the effect more clearly. The images are shown at 0.20 ms ASOI, which corresponds to 20% of the injection duration. The liquid jets at the top half of the images appear less intense since the LED was illuminating from the bottom to top. The electric signal to trigger the injector was fixed at the same crank angle for both engine speeds, leading to a 16% gas-density increase at 2000 rpm, for the crank angle when these particular images were recorded. Of course it is not possible to separate the effect of the 16% increase in density from the flow speed between the two engine speeds. However, both effects are present for normal engine conditions and the inability to separate these two effects does not detract from the observed increase in variability of the liquid jets at 2000 rpm. Images from three different cycles are shown for each condition with an overlay for reference, showing the expected direction of the spray jets based on averaged images. At each condition, the left-most image was chosen to have the most symmetric jet orientation and undistorted individual jets. The other two show distorted sprays. These still images do not reveal the dramatic change in the cycle-to-cycle variability between 333 and 2000 rpm observed when watching animations of multiple cycles. However, careful inspection of these individual cycles does show characteristic features of the distortion. One is the variability of the 11:00- and 1:00-jet tips adjacent to the ground strap (compare a2 to a3 and b2 to b3). In some cycles the tips may be splayed away from or into the ground strap. Other notable features include tip penetration, individual jet spread (width), and jet coalescence. These features were observed at both engine speeds, but were more extreme and more prevalent at 2000 rpm and the relatively undistorted images of a1 and b1 were less frequent at 2000 rpm. Additionally, the animations showed that the spray jets appeared to rotate in unison from cycle to cycle at 2000 rpm.

This spray imaging reveals that the in-cylinder flow field generated by the intake and compression strokes becomes sufficiently strong that it directly impacts the liquid structure of both the individual fuel jets and the overall spray pattern, thereby causing elevated cycle-to-cycle variations. These observations are consistent with the increased combustion variability observed at 2000 rpm.

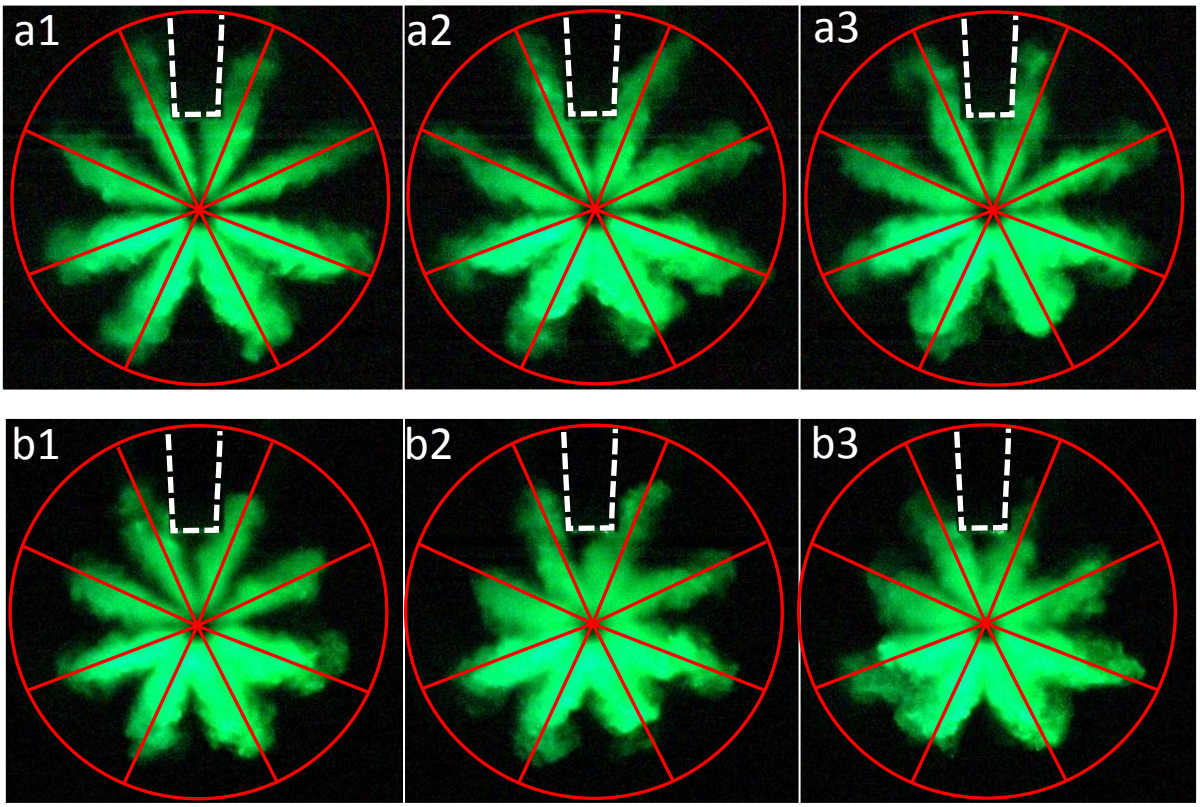

Figure 20 - Individual-cycle scattered-light images of the liquid spray for two engine speeds. The overlay is for reference and indicates the expected jet trajectories based on averaged images. (a) Liquid SOI = -22.2°CA ATDC, images recorded 0.20 ms = 0.4°CA after liquid SOI at 333 rpm. (b) Liquid SOI = -18.6°CA ATDC, images recorded 0.20 ms = 2.4°CA ASOI at 2000 rpm.

5. Summary and conclusions

Previous studies demonstrated the benefits of high ethanol fuel (>E70) for spray-guided direct-injection stratified-charge combustion [3, 4]; namely, low soot and low NO_x compared to pure gasoline but limited by the onset of partial burns. The improved emissions were made possible by the use of late injection and ignition of the head of the ethanol spray, not viable with gasoline. Using E70 fuel in [9], it was observed that as the engine speed increased from 1000 to 2000 rpm, the time-based combustion rates increased but much less than for spark-ignited homogeneous combustion. This led to the first hypothesis, that the combustion rate is primarily governed by the fuel/air-mixing rates, and that this mixing is mostly driven by the spray. However, the cycle-to-cycle variability of combustion increased with engine speed, leading to the second hypothesis that at higher speeds the in-cylinder flow field becomes a significant contributor to the hypothesized mixing-dominated burning rate. Those results motivated this optical study that is intended to isolate the roles of the in-cylinder gas flow versus the spray-induced flow.

Combustion analysis of the skip-fired E70 stratified-charge DISI operation in this optical engine demonstrate the same combustion characteristics as the continuously fired metal engine operation [9] when increasing the engine rpm. Of course, the flow-induced change of combustion due to the rpm increase is confounded by difference in the thermodynamic (T, P) rate of change (in °CA) during the injection, which has a constant time duration (in ms). Thus, high-speed particle image velocimetry (PIV) is used to quantify properties of the flow, independently. In addition to the visualization of the mean and cyclic variability of the flow structures, the in-cylinder gas flow momentum (average and cyclic variability) is quantified by the per cycle spatially averaged flow speed. For the purposes of this study, the flow velocity was measured without combustion, with and without fuel injection. In addition, high-speed imaging of scattered light is used to reveal the effects of the flow on the liquid spray.

The PIV measurements reveal that, without injection, the ensemble-averaged velocity distributions appear similar and the magnitudes scale linearly between 1000 and 2000 rpm, as expected. With injection, the gas flow is dominated by the entrainment generated by the spray. However, at 2000 rpm individual-cycle images reveal that, for cycles with large measured velocities just prior to injection, the gas-phase flow structure can persist less altered by the spray. The data reveal that the ensemble-averaged flow speed (momentum) without injection at 2000 rpm is indeed twice that of 1000 rpm. Further, the magnitude of the speed variability from cycle to cycle is significantly greater at 2000 rpm, prior to injection. Fuel injection causes the average flow speed to increase by a similar magnitude for each speed. The net effect of the speed change from 1000 to 2000 rpm is that the average flow speed after injection increases by 24%. The fuel injection also reduces the cycle-to-cycle variability of the flow after injection, both in absolute and relative terms. This demonstrates that the liquid spray does indeed have a dominant effect on the flow but that the flow generated by the intake stroke contributes to the cyclic variability of the flow momentum.

Additional high-speed imaging was performed for the duration of the injection event for 200 cycles at both 333 rpm (a more quiescent gas flow) and 2000 rpm. The images reveal that the eight spray jets can rotate in unison from cycle, coalesce (or not) and take independent trajectories. The variability is significantly higher at 2000 rpm. Together with the measured velocity results, it can be concluded that the two hypotheses are correct; The flow, fuel/air mixing and combustion rate are dominated by the spray, but the intake-generated gas flow contains sufficient momentum to affect fuel/air-mixing and thereby cause cycle-to-cycle variability of the stratified combustion, especially at higher speeds. Furthermore, these observations suggest that, in future work, it may be worthwhile to examine the relationship between flow field, liquid fuel penetration, gas-phase fuel distribution and combustion on a per-cycle basis.

References

1. Solomon, S., Qin, D., Manning, M., Chen, Z., et al. (eds.), “Contribution of Working Group I to the Fourth Assessment Report of the Intergovernmental Panel on Climate Change”, Cambridge University Press, Cambridge, United Kingdom and New York, NY, USA, 2007.
2. Schwarz, C., Schünemann, E., Durst, B., Fischer, J. et al., "Potentials of the Spray-Guided BMW DI Combustion System," SAE Technical Paper 2006-01-1265, 2006, doi: 10.4271/2006-01-1265.
3. Sjöberg, M., Reuss, D.L., “High-speed Imaging of Spray-guided DISI Engine Combustion with Near-TDC Injection of E85 for Ultra-low NO and Soot”, Proceeding of the Combustion Institute, 34(2):2933-2940, 2013, doi: 10.1016/j.proci.2012.05.033.
4. Sjöberg, M. and Reuss, D., "NOx-Reduction by Injection-Timing Retard in a Stratified-Charge DISI Engine using Gasoline and E85," SAE Int. J. Fuels Lubr. 5(3):1096-1113, 2012, doi: 10.4271/2012-01-1643.
5. Drake, M.C., Fansler, T.D., and Lippert, A.M., “Stratified-charge Combustion: Modeling and Imaging of a Spray-guided Direct-injection Spark-Ignition Engine”, Proceedings of the Combustion Institute, 30(2):2683-2691, 2005, doi:10.1016/j.proci.2004.07.028.
6. Honda, T., Kawamoto, M., Katashiba, H., Sumida, M. et al., "A Study of Mixture Formation and Combustion for Spray Guided DISI," SAE Technical Paper 2004-01-0046, 2004, doi: 10.4271/2004-01-0046.

7. Schwarz, C., Schünemann, E., Durst, B., Fischer, J. et al., "Potentials of the Spray-Guided BMW DI Combustion System," SAE Technical Paper 2006-01-1265, 2006, doi: 10.4271/2006-01-1265.
8. Heywood, J.B., *Internal Combustion Engine Fundamentals*, McGraw-Hill, New York, 1988.
9. Sjöberg, M., Zeng. W., and Reuss, D. "Role of Engine Speed and In-cylinder Flow Field for Stratified and Well-mixed DISI Engine Combustion using E70", draft manuscript submitted to SAE Congress 2014, paper offer #14PFL-468.
10. Fansler, T.D., Stojkovic, B., Drake, M.C., and Rosalik, M.E., "Local Fuel Concentration Measurements in Internal Combustion Engines using Spark-emission Spectroscopy", Applied Physics B, 75(4-5):577-590, 2013, doi: 10.1007/s00340-002-0954-0.
11. Fansler, T.D., Drake, M.C., Düwel, L., and Zimmermann, F.P., "Fuel-spray and Spark Plug Interactions in Spray-guided Direct-injection Gasoline Engine", Proceedings of the Seventh International Symposium on Internal Combustion Diagnostics, Baden-Baden, Germany, 81-97, 2006.
12. Fansler, T.D., Drake, M.C., and Böhm, B., "High-speed Mie-scattering Diagnostics for Spray Guided Gasoline Engine Development", Proceedings of the Eight International Symposium on Internal Combustion Diagnostics, Baden Baden, Germany, 413-425, 2008.
13. Peterson, B., Reuss, D.L and Sick, V., "High-speed Imaging Analysis of Misfires in a Spray-guided Direct Injection Engine", Proceedings of the Combustion Institute, 33(2):3089-3096, 2011, doi: 10.1016/j.proci.2010.07.079.
14. Zeng, W., Xu, M., Zhang, M., Zhang, Y., and Cleary, D.J., "Macroscopic Characteristics for Direct-injection Multi-hole Sprays using Dimensionless Analysis", Experimental Thermal and Fluid Science, 40:81-92, 2012, doi: 10.1016/j.expthermflusci.2012.02.003.
15. Zeng, W., Xu, M., Zhang, G., Zhang, Y., and Cleary, D.J., "Atomization and Vaporization for Flash-boiling Multi-hole Sprays with Alcohol Fuels", Fuel, 95:287-297, 2012, doi: 10.1016/j.fuel.2011.08.048.
16. Zeng, W., Xu, M., Zhang, M., Zhang, Y., and Cleary, D.J., "Characterization of Methanol and Ethanol Sprays from Different DI Injectors by Using Mie-scattering and Laser Induced Fluorescence at Potential Engine Cold-start Conditions," SAE Technical Paper 2010-01-0602, 2010, doi:10.4271/2010-01-0602.
17. Miles, P.C., "Turbulent Flow Structure in Direct-Injection, Swirl-Supported Diesel Engines", Chapter 4, *Flow and Combustion in Reciprocating Engines*, Springer-Verlag Berlin Heidelberg,173-256, 2009, doi: 10.1007/978-3-540-68901-0_4.
18. ASTM Standard D5798-11, "Standard Specification for Ethanol Fuel Blends for Flexible-Fuel Automotive Spark-Ignition Engines", June 2011.
19. US Energy Policy Act of 1992 (Title III, Sec. 301).
20. Fajardo, C. and Sick, V., "Flow Field Assessment in a Fired Spray-guided Spark-ignition Direct-injection Engine based on UV Particle Image Velocimetry with Sub Crank Angle Resolution", Proceedings of the combustion institute, 31(2)3023-3031, 2007, doi: 10.1016/j.proci.2006.08.016
21. Adrian, R.J. and Westerweel, J., Particle Image Velocimetry, Cambridge University Press, New York, 2010
22. Megerle, M., Sick, V. and Reuss D.L, "Measurement of Digital Particle Image Velocimetry Precision using Electro-optically Created Particle-Image Displacements", Measurement Science and Technology, 13:997, 2002, doi:10.1088/0957-0233/13/7/305.
23. Abraham, P., Reuss, D., and Sick, V., "High-Speed Particle Image Velocimetry Study of In-Cylinder Flows with Improved Dynamic Range," SAE Technical Paper 2013-01-0542, 2013, doi: 10.4271/2013-01-0542.
24. Drake, M.C, Fansler, T.D., and Peterson, K.H., "Stratified Ignition Process in Spray-Guided SIDI Engines", Proceedings of the Eight International Symposium on Internal Combustion Diagnostics, Baden Baden, Germany, 8-19, 2010.
25. Zeng, W., Idicheria, C., Fansler, T., and Drake, M., "Conditional Analysis of Enhanced Combustion Luminosity Imaging in a Spray- Guided Gasoline Engine with High Residual Fraction," SAE Technical Paper 2011-01-1281, 2011, doi: 10.4271/2011-01-1281.
26. Borée, J. and Miles, P.C., "In Cylinder Flow", Article 119 in the *Encyclopedia of Automotive Engineering* Online, John Wiley & Sons, Ltd., 2014, doi: 10.1002/9781118354179.auto119

Acknowledgments

The authors would like to thank Alberto Garcia, Gary Hubbard, Ken St. Hilaire, Keith Penney, and Sal Birtola for their dedicated support of the DISI laboratory. Chris Carlen should be acknowledged for developing the high-intensity LEDs. Also, thanks to Paul Miles for helpful discussions and feedback on the manuscript.

The work was performed at the Combustion Research Facility, Sandia National Laboratories, Livermore, CA. Financial support was provided by the U.S. Department of Energy, Office of Vehicle Technologies. Sandia is a multiprogram laboratory operated by the Sandia Corporation, a Lockheed Martin Company, for the United States Department of Energy's National Nuclear Security Administration under contract DE-AC04-94AL85000.

Contact Information

Wei Zeng, wzeng@sandia.gov
Engine Combustion Department
Combustion Research Facility
Sandia National Laboratories
MS 9053, PO Box 969
Livermore, CA 94551-0969
USA